Redox Biology 81 (2025) 103577

Contents lists available at ScienceDirect

Redox Biology

journal homepage: www.elsevier.com/locate/redox

3D Histology visualizing hypoxia-induced upregulation of *N*-terminal cysteine using *de novo* fluorophore generation

Yunjung Choi [a,1], Joo-Yeong Jeon [b,1], Jeongin Hwang [a], Sejong Choi [a], Ki-Myo Kim [c], Ji-Ung Park [c,*], Yan Lee [a,d,**]

[a] Department of Chemistry, Seoul National University, Seoul, 08826, South Korea
[b] Korea Basic Science Institute (KBSI), Seoul, 02841, South Korea
[c] Department of Plastic and Reconstructive Surgery, Seoul National University Boramae Hospital, Seoul National University College of Medicine, Seoul, 07061, South Korea
[d] School of Transdisciplinary Innovations, Seoul National University, Seoul, 08826, South Korea

ARTICLE INFO

Keywords:
N-terminal cysteine
Arg/*N*-degron pathway
Hypoxia-related disease diagnosis
Histopathology
Tissue imaging
3D imaging

ABSTRACT

Our research group developed a novel fluorescence staining strategy based on the DNFC targeting *N*-Cys in proteins. By treating biological samples with non-fluorogenic citrate and coupling reagents, we achieved strong cyan fluorescence, enabling effective visualization of *N*-Cys proteins in cells and tissues. The DNFC reaction occurs specifically on *N*-Cys residues, making it highly ideal for monitoring protein processing events, particularly within the Arg/*N*-degron pathway. Under hypoxic conditions, DNFC fluorescence is significantly enhanced, likely due to the increased presence of *N*-Cys-containing proteins. Using immunoassays and mass spectrometry, we identified Class 2 actin as a target protein under hypoxia, emphasizing the utility of 3D histopathology for analyzing actin's spatial distribution. Furthermore, we have identified a novel finding indicating a significant presence of RGS5 in red blood cells (RBCs), a discovery that has not been previously reported. Our fluorescence imaging studies, conducted across various cell types, animal tissues, and human clinical samples suggest that DNFC staining, when combined with tissue-clearing techniques, enables detailed 3D imaging of *N*-Cys proteins and may offer a means to assess molecular responses to hypoxia within tissues. This study highlights the potential of DNFC as a valuable tool for imaging and quantitative analysis of *N*-proteomes and providing a foundation for 3D histopathology in hypoxia-related disease research.

1. Introduction

Fluorescent staining is essential for fluorescence-based imaging, enabling the visualization of molecular distribution and activity within biological systems [1,2]. Certain fluorescent probes can non-specifically or semi-specifically bind to biomolecules, providing insights into general biological structures [3]. Additionally, fluorophores can be conjugated to ligands such as antibodies [4], aptamers [5,6], or peptides [7,8], enabling specific recognition and visualization of target molecules of interest. for specific recognition of target molecules.

Advanced techniques such as super-resolution microscopy [9,10] and tissue clearing [11,12] enable three-dimensional (3D) analysis and detailed visualization of stained biological tissues, overcoming the spatial resolution limitations of optical microscopy.

Most conventional fluorescent staining methods rely on pre-synthesized fluorophores. Chemical and biological fluorophores, such as cyanine, rhodamine, and coumarin, are widely used for labeling, but these often bind non-specifically unless equipped with reactive functional groups. Chemical fluorophores with reactive groups like *N*-hydroxysuccinimide ester or maleimide typically lack chemoselectivity and can be expensive due to complex synthesis processes. This limitation restricts their application, especially for staining large tissue samples [13,14].

Recently, our group has developed a novel staining method based on citrate, a simple tricarboxylate metabolite [15,16]. Citrate has been reported to react with certain amine-based molecules, resulting in the

* Corresponding author.
** Corresponding author. Department of Chemistry, Seoul National University, Seoul, 08826, South Korea.
E-mail addresses: alfbskan@gmail.com (J.-U. Park), gacn@snu.ac.kr (Y. Lee).
[1] These authors contributed equally to this work.

https://doi.org/10.1016/j.redox.2025.103577
Received 16 January 2025; Received in revised form 18 February 2025; Accepted 26 February 2025
Available online 3 March 2025

formation of fluorophores [17,18]. Specifically, citrate can react with L-cysteine (Cys) to produce a fluorophore, 5-oxo-2,3-dihydro-5H- [1,3] thiazolo [3,2-a]pyridine-3,7-dicarboxylic acid (TPA), (Fig. S1) [18]. Traditionally, the fluorophore was generated under harsh conditions at high temperatures (100–150°C) [17–19]. However, our group was able to facilitate fluorophore formation even at 25–37°C by using amide coupling reagents and successfully applied this reaction to biological sample staining [20]. Remarkably, without relying on pre-synthesized fluorophores, we achieved strong cyan fluorescence in cells and tissues simply by treating them with non-fluorogenic citrate and the coupling reagents and observed detailed biological structures by fluorescence microscopy. Moreover, when combined with tissue-clearing techniques, our method allowed us to effectively visualize the general morphology of thick tissue samples in 3D. We could also extract various volumetric information from the resulting 3D images [21]. Because our approach is based on *De Novo* Formation of Citrate-based fluorophores (DNFC), the cost-effective staining method was denominated as DNFC staining. In this study, we investigate the conditions under which DNFC is more effectively facilitated and identify the specific target proteins that are more susceptible to this labeling method.

Because both neighboring amino and thiol residues are required to generate the TPA structure emitting cyan fluorescence, we anticipate that the DNFC straining can predominantly produce the cyan fluorophore at the *N*-Cys residues of proteins possessing both α-amino and β-thiol groups in their structure (Fig. 1a). In this study, we initially investigate whether fluorophore generation depends quantitatively on

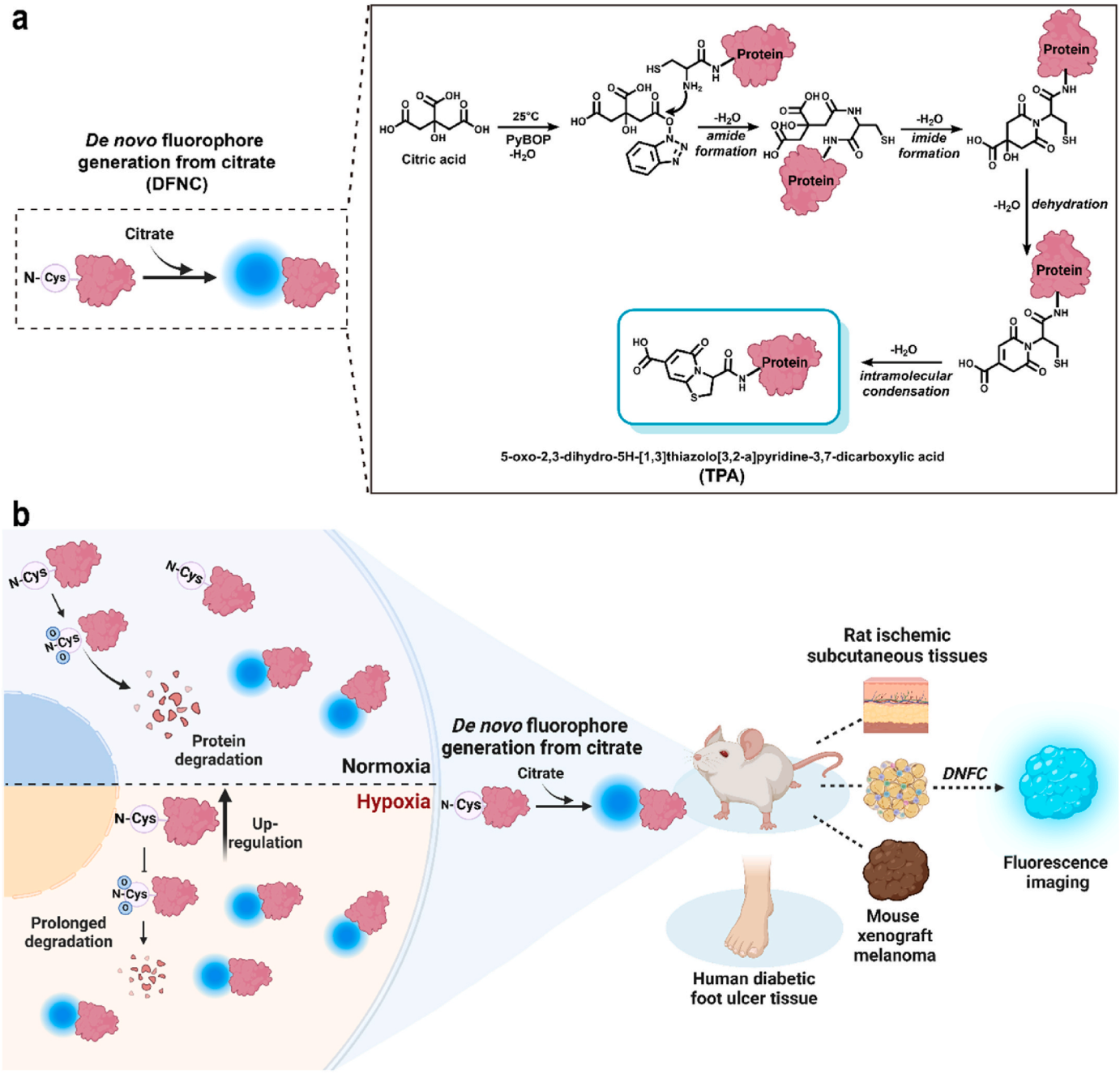

Fig. 1. A proposed mechanism and schematic overview of DNFC. (a) A proposed mechanism for the generation of a citrate-based fluorophore, TPA, on *N*-terminal cysteines facilitated by coupling reagents. (b) Schematic representation for the citrate-based fluorophore generation on the proteins with *N*-terminal cysteines up-regulated in hypoxic tissues.

N-Cys residues. Across various levels–amino acids, peptides, proteins and cells–we aim to confirm that fluorescence intensity correlates with abundance of *N*-Cys residues in biological samples. The selective fluorophore generation suggests its potential effectiveness in visualizing and quantifying *N*-Cys residues which are exposed by post-translational modifications [22,23]. While the biological role of *N*-Cys in proteins remains incompletely understood, we infer a possible relationship between *N*-Cys and redox potential within the biosystem considering the well-known Arg/*N*-degron pathway, where *N*-Cys undergoes oxidation and subsequent arginylation leading to protein degradation [24,25]. Notably, after observation of remarkably enhanced fluorescence intensity in various cells and tissues under hypoxic conditions, we propose possible mechanisms of up-regulated *N*-Cys during hypoxia (Fig. 1b). Furthermore, we present a methodology for visualizing the general morphology of tissues and estimating hypoxic status in 3D manners by integrating DNFC staining with tissue clearing techniques. Collectively, we suggest that DNFC staining holds promise as a tool for fluorescence imaging and quantitative analysis of proteins with *N*-Cys in biological specimens. Its potential extends to investigating the unknown roles and distributions of proteins with *N*-Cys, particularly in the context of hypoxia, and advancing 3D histopathology for various hypoxia-related diseases.

2. Results and discussion

2.1. De novo fluorophore generation from citrate and Cys

Previous studies conducted by Yang's group demonstrated that fluorescence characteristics could be produced in polymers by reaction with citrate and amino acids under heating conditions at 100–150°C [19]. Among various amino acids, Cys showed the strongest fluorescence by the reaction with citrate. Kasprzyk's group confirmed that the fluorescence originated from the TPA structure which possesses a fused thiazolopyridine ring. TPA emits strong fluorescence (λ_{abs} = 365 nm, λ_{em} = 440 nm, $\varepsilon > 8000\ M^{-1}\ cm^{-1}$ and $\phi_F > 80\%$) with high photostability [17]. (Fig. 2a). In a previous study, our group could facilitate

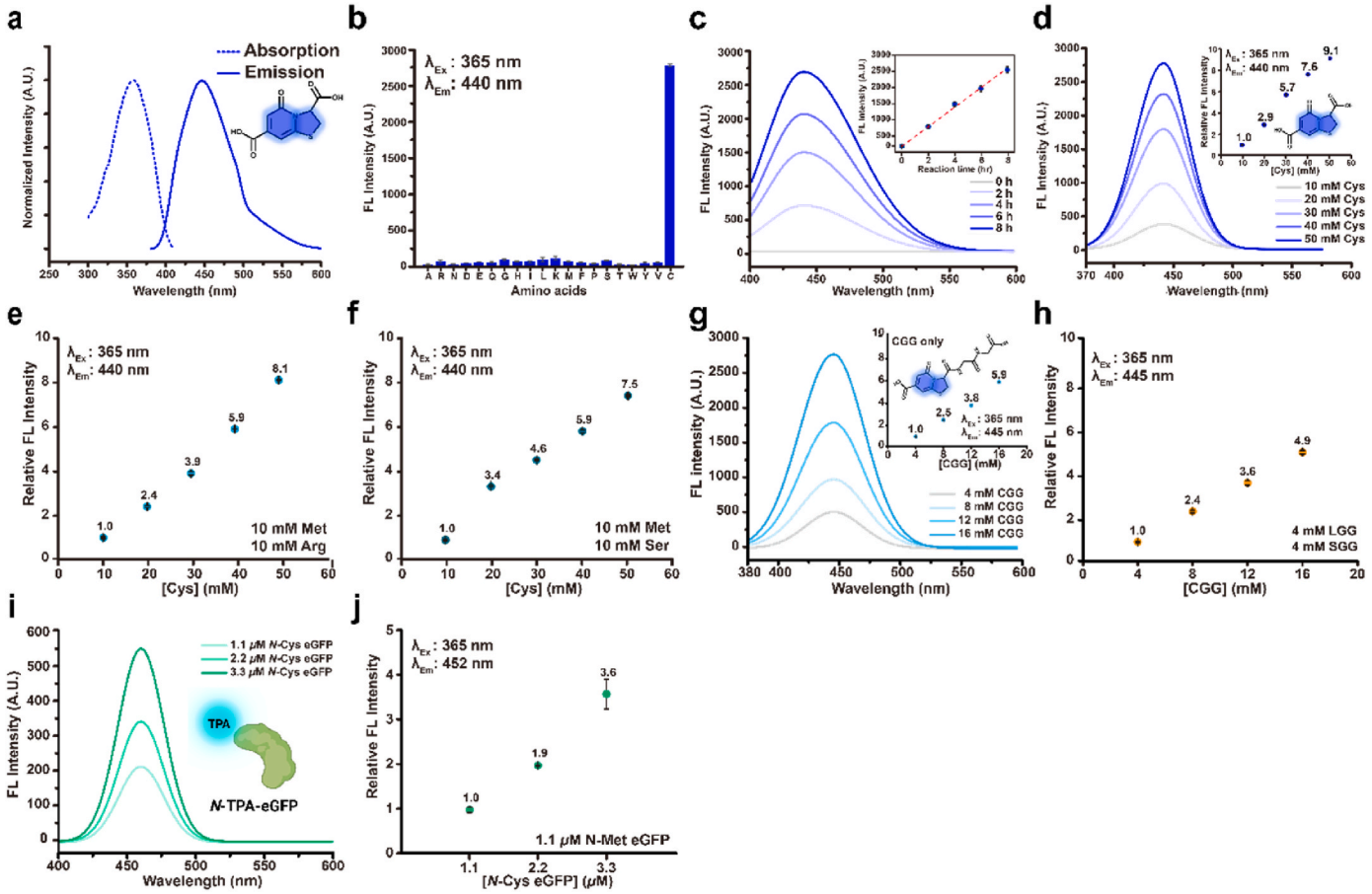

Fig. 2. [Cys]-dependent generation of TPA in various bio-**mixtures.** (a) The absorption (dashed line) and emission (solid line) spectra of TPA, which is measured in 75% (v/v) DMSO (60 μM) at T = 298 K. (b) Fluorescence intensity of amino acid/Cit mixtures after 24 h-incubation with PyBOP in DMSO. The molar ratio of amino acid: Cit: PyBOP was fixed as 1 : 1: 1, respectively. (c) Time-dependent generation of the fluorescence in a Cys/Cit mixture with PyBOP in DMSO. The fluorescence spectra have been deconvoluted. The change of the fluorescence intensity at 440 nm was plotted in the inset graph. [Cys], [Cit], and [PyBOP] were 0.24 M. The emission spectra were obtained by excitation at 365 nm. (d) [Cys]-dependent generation of the fluorescence in Cys/Cit mixtures with PyBOP in DMSO after 24 h. The relationship of [Cys] and the relative fluorescence intensity at 440 nm was plotted in the inset graph. The fluorescence spectra have been deconvoluted. The relationship between [Cys] and the fluorescence intensity of Cys/Cit mixtures (e) with methionine (10 mM) and arginine (10 mM) and (f) with methionine (10 mM) and serine (10 mM), after 24 h-incubation with PyBOP in DMSO. [Cit] and [PyBOP] were fixed as 0.24 M and 0.24 M, respectively. (g) The deconvoluted fluorescence spectra of CGG peptide/Cit mixtures without any additional tripeptide. The relationship of [CCG] and the relative fluorescence intensity at 440 nm of the mixture was plotted in the inset graph. The spectra were obtained by excitation at 365 nm. (h) The relationship between [CGG] and the relative fluorescence intensity of the mixtures containing CGG, LGG (4 mM) and SGG (4 mM), after 24 h-incubation with PyBOP in 75% DMSO/water. (i) The deconvoluted fluorescence spectra of *N*-Cys eGFP/Cit mixtures after 24 h-incubation with PyBOP in 75% DMSO/water. The concentration of *N*-Cys eGFP (*N*-Cys eGFP) was varied in the mixture. The spectra were obtained by excitation at 365 nm. (j) The relationship between [*N*-Cys eGFP] and the fluorescence intensity (452 nm) of eGFP/Cit mixtures after 24 h-incubation with PyBOP in 75% DMSO/water. In the experiment, *N*-Met eGFP (3.2 μM) was also added to the mixture. Each error bar represents S.D. (n = 3).

the TPA formation at 25–37°C by utilizing an amide coupling reagent (PyBOP) [20].

Initially, we assessed whether DNFC fluorescence generation depends on cysteine (Cys) rather than other amino acids. Among the 20 α-amino acids tested, only Cys demonstrated significantly higher fluorescence intensity following DNFC treatment (Fig. 2b and Fig. S2a). Additionally, when comparing the fluorescence spectra of n-butylamine, ethanolamine, and cysteamine after DNFC treatment, only cysteamine exhibited strong fluorescence emission comparable to the Cys mixture (Fig. S2b). This underscores the essential roles of both α-amino and β-thiol groups in fluorophore generation. Accordingly, homocysteine, which possess α-amino and γ-thiol groups, did not exhibit fluorescence (Fig. S2c). A small fluorescence emission peak was observed at around λ_{em} = 460–470 nm in all DNFC-treated mixtures, which is likely to originate from the PyBOP-activated citrate. We also observed that the fused ring structure was not formed after the DNFC treatment of non-Cys amino acids by the LC-MS analysis. Therefore, we propose that only Cys could form the fused thiazolopyridine ring structure for strong fluorescence generation under the DNFC condition (Fig. 1a and Fig. S1).

There was a noticeable time dependence in the generation of DNFC fluorescence (Fig. 2c and Fig. S3). With a fixed concentration of cysteine ([Cys]), fluorescence intensity at λ_{em} = 440 nm increased linearly over time, while [Cys] exhibited a linear correlation with DNFC fluorescence (Fig. 2d), facilitating quantitative analyses in biological mixtures.

2.2. Fluorophore generation is highly selective for N-Cys across multiple biological mixtures

We examined whether the fluorescence is quantitatively developed according to [Cys] in various mixtures including amino acids, peptides, and proteins, by the DNFC treatment. This study aimed to understand the relationship between Cys concentration and fluorescence intensity across different biological contexts, facilitating a comprehensive analysis of the DNFC process. Initially, we assessed the development of the DNFC fluorescence in mixtures containing Cys and other amino acids. L-methionine (Met), L-arginine (Arg) and L-serine (Ser) were selected as representative amino acids. In a mixture of Cys, Met, and Arg, the fluorescence intensity at 440 nm increased in a linear manner as the [Cys] increased (Fig. 2e and Fig. S3). In another mixture of Cys, Met, and Ser, the similar [Cys]-dependence of the fluorescence intensity was observed (Fig. 2f and Fig. S3). Notably, the results highlighted that the development of fluorescence was predominantly dependent on the concentration of Cys alone, with no significant influence from the other amino acids present in the mixtures. Next, we measured the fluorescence development at the level of peptides. After preparation of tripeptides with different *N*-termini, cysteine-glycine-glycine (CGG), leucine-glycine-glycine (LGG), and serine-glycine-glycine (SGG), the tripeptide mixture were treated by the DNFC process with varying the concentration of CGG. In the peptide mixture, the maximum emission was observed at 445 nm (Fig. 2g and Fig. S4). It is hypothesized that this slight red shift of the emission is attributed to the elongation of the side branch through the amide bond formation between TPA structure and the next amino acid (glycine). Similar to the amino acid mixtures, the fluorescence intensity at 445 nm increased in a linear manner according to the concentration of CGG in the peptide mixture (Fig. 2h and Fig. S4). Peptides with *N*-terminal cysteine can generate the DNFC fluorescence in a linear manner according to the concentration even in more complex biological mixtures such as cell lysates (Fig. S4).

Furthermore, we also intended to know whether the DNFC fluorescence development was observed in a quantitative manner at the level of proteins with various reactive side chains in the sequence. For the preparation of model proteins with different *N*-terminal amino acids, we used a pH intein sequence, which induces the self-cleavage of protein according to the pH variation [26]. As a result, we obtained eGFP with *N*-terminal Met (*N*-Met-eGFP) and Cys (*N*-Cys-eGFP), respectively (Fig. S5a). Although eGFP shows its own fluorescence at 512 nm, the DNFC treatment could generate a new fluorescence peak at 452 nm (Fig. 2i and Fig. S5b). *N*-Cys-eGFP exhibited a clear positive correlation between its concentration and the DNFC fluorescence intensity (Fig. 2j), whereas the addition of *N*-Met-eGFP lead no increase of fluorescence at 452 nm (Fig. S5c). These findings suggest a notably positive correlation between the DNFC fluorescence and the amount of *N*-Cys at the protein level. Therefore, we believe that the DNFC process could be employed for quantification of *N*-Cys of proteins in complex biological mixtures such as cells or tissues.

2.3. Quantitative DNFC staining of exogenous N-Cys in HeLa cells

In this study, we initiated the application of DNFC for the quantitative evaluation of *N*-Cys in biological samples by measuring the fluorescence intensity of *HeLa* cells post-DNFC staining (Fig. S6). Since TPA emits broad cyan fluorescence with the maximum emission wavelength of 490 nm by excitation with blue laser (λ_{ex} = 405 nm), we obtained the confocal laser scanning microscope (CLSM) images of the DNFC-stained *HeLa* cells in the wavelength range of 410–550 nm and analyzed them by the ImageJ program.

HeLa cells showed almost negligible autofluorescence in this condition before the DNFC staining, whereas they showed strong cyan fluorescence after the DNFC staining (Fig. 3a). It is highly plausible that the developed cyan fluorescence originated from endogenous proteins with *N*-Cys in the cells.

To enhance the expression of *N*-terminal cysteine (*N*-Cys) proteins, *HeLa* cells were transfected with a plasmid designed to express maltose-binding protein (MBP) with *N*-Cys (*N*-Cys-MBP) using a self-cleavable pH intein linker [26]. *HeLa* cells were transfected with a plasmid intended to express maltose-binding protein (MBP) with *N*-Cys (*N*-Cys-MBP) via a self-cleavable pH intein linker in order to increase the expression of *N*-Cys proteins. When compared to non-transfected controls, cells producing MBP with *N*-Cys-MBP displayed a fluorescence intensity increase of almost two times (Fig. 3b and d). In contrast, cells transfected with *N*-Met-MBP did not exhibit any significant alterations. The cytoplasm was where magenta-stained MBPs were mostly found, according to anti-MBP antibody staining. Notably, *N*-Cys-MBP-transfected cells showed noticeably increased DNFC fluorescence in the nucleus and cytoplasm, suggesting that *N*-Cys sites are primarily responsible for DNFC fluorophore production. Anti-MBP antibody staining revealed that magenta-stained MBPs were primarily localized in the cytoplasm. Notably, *N*-Cys-MBP-transfected cells displayed significantly enhanced DNFC fluorescence in both the cytoplasm and nucleus, indicating that DNFC fluorophore generation occurs predominantly at *N*-Cys sites (Fig. 3c and Fig. S7).

Taken together, we confirmed that the DNFC staining could successfully generate the cyan fluorescence in the cells and that the fluorescence level and distribution are highly correlated with the expression of *N*-Cys proteins in the cells.

2.4. Hypoxia-induced elevation of DNFC fluorescence is likely mediated by the Arg/N-degron pathway

We confirmed that the DNFC signal changes quantitatively in response to the number of *N*-Cys proteins. Protein translation starts from *N*-Met but certain *N*-terminal amino acid sequences are trimmed or modified for cellular trafficking or controlling half-lives of the proteins [27]. *N*-Cys could be exposed through such post-translational trimming or modification. Possibly, the level of the exposed *N*-Cys could be delicately controlled according to the intracellular redox potential, because the thiol groups are highly vulnerable in oxidative environments [28]. Among various *N*-terminal modification pathways that have been discovered, we focused on the Arg/*N*-degron pathway (Fig. S8 and Table S1), by which the oxidized *N*-Cys is recognized and modified with arginine for facilitating the protein degradation [24]. Therefore, we expected that the intracellular DNFC fluorescence intensity can be

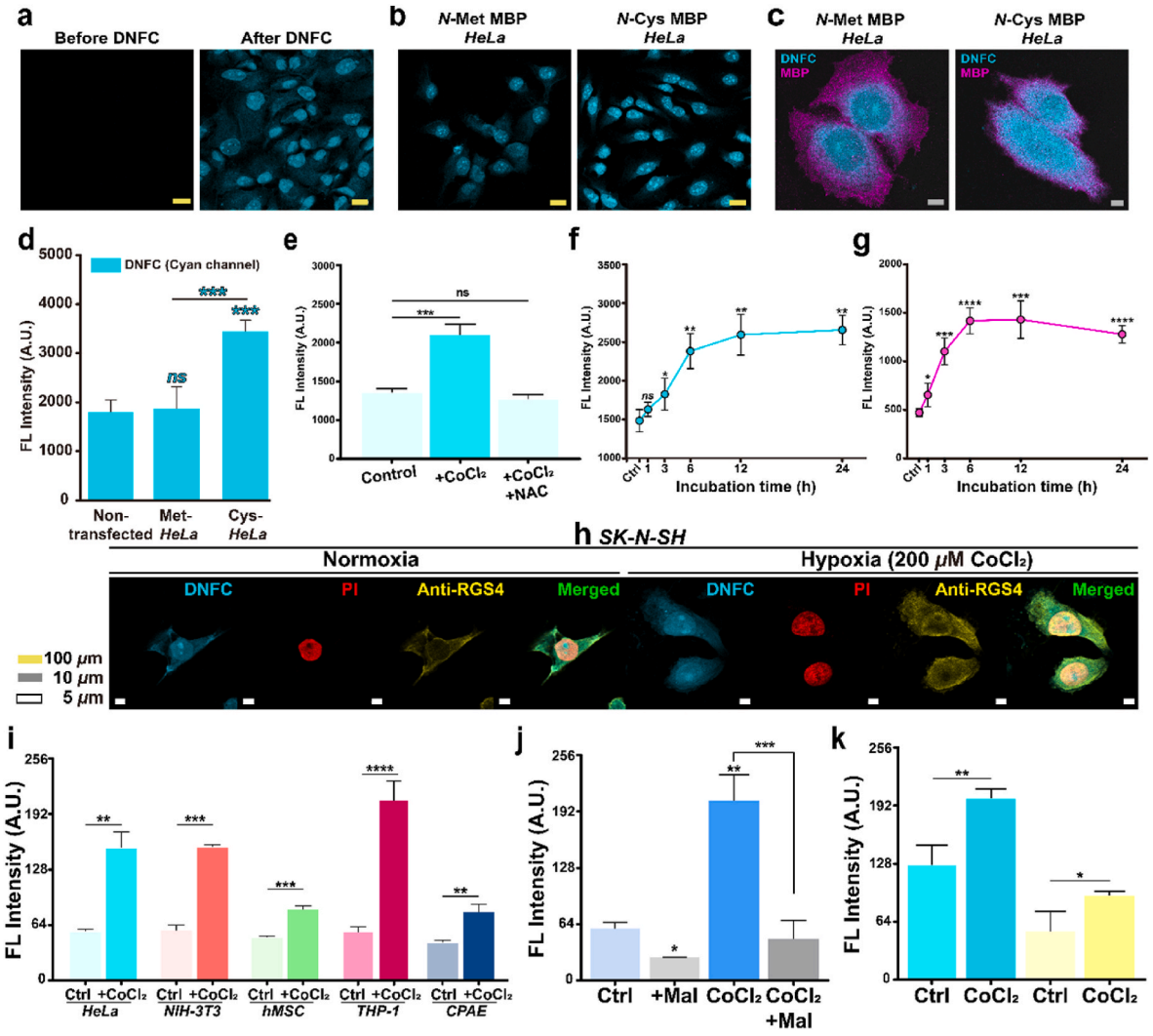

Fig. 3. Enhancement of DNFC fluorescence in *HeLa* cells by hypoxia induction. (a) Representative CLSM images of non-transfected *HeLa* cells before and after DNFC staining. (b) Representative CLSM images of DNFC-stained *HeLa* cells which were initially transfected with plasmids expressing MBP with *N*-terminal methionine (*N*-Met MBP) and MBP with *N*-terminal cysteine (*N*-Cys MBP), respectively. (c) Merged cyan- and magenta-channel images of DNFC-stained *HeLa* cells expressing two MBPs. (d) Comparison of DNFC (cyan) fluorescence intensity of *HeLa* cells before and after the plasmid transfection. The fluorescence of three images with more than 100 cells was measured and averaged ($n = 3$). (e) Cyan fluorescence intensity of DNFC-stained *HeLa* cells in normoxic and hypoxic ($CoCl_2$) conditions. *N*-acetyl L-cysteine (NAC) was treated for inhibition of reactive oxygen species (ROS). (f) Time-course of cyan fluorescence intensity of DNFC-stained *HeLa* cells after the hypoxia induction. (g) Time-course of the expression of the hypoxia marker, HIF-1α, in *HeLa* cells after the hypoxia induction. The hypoxic condition was induced by treatment of $CoCl_2$ (200 μM). The fluorescence of three images with more than 100 cells was measured and averaged ($n = 3$). (h) Magnified images of *SK-N-SH* cells under normoxia and hypoxia conditions. (i) Comparison of DNFC fluorescence intensity of various cells in normoxic and hypoxic conditions. (j) The effect of the maleimide (MaI) treatment on the DNFC fluorescence intensity of *THP-1* cells. (k) Comparison of DNFC (cyan) and RGS4 (yellow) fluorescence intensity of *SK-N-SH* cells in normoxic and hypoxic conditions. Each error bar represents S.D. *, **, ***, and **** indicate $0.01 \leq p < 0.05$, $0.001 \leq p < 0.01$, $0.0001 \leq p < 0.001$ and $p < 0.0001$, respectively. ns indicates no significant difference compared to the control.

changed by the redox stresses.

Since hypoxic conditions dramatically affects the intracellular redox potential [29], we examined the change of the DNFC fluorescence intensity of *HeLa* cells in hypoxia. After treatment of a hypoxia-inducing reagent ($CoCl_2$) for 24 h, *HeLa* cells exhibited approximately 1.6-fold higher DNFC fluorescence intensity compared to the cells in normoxic conditions (Fig. 3e). When a reactive oxygen species (ROS) scavenger (*N*-acetyl cysteine) was additionally treated to the $CoCl_2$-treated cells, the DNFC fluorescence intensity decreased to the level of the cells in normoxic conditions, which implies the role of ROS for the increase of *N*-Cys.

The increase of the DNFC fluorescence is highly correlated with the amount of hypoxia-inducible factor-1α (HIF-1α). The time-courses of the DNFC fluorescence intensity and the HIF-1α after the $CoCl_2$ treatment are shown in Fig. 3f and g. The saturation of the DNFC fluorescence intensity reflecting the amount of *N*-Cys was slightly behind the saturation of HIF-1α. The hypoxia induction, which is associated with the expression of HIF-1α, might alter the protein metabolism to increase the *N*-Cys level in the proteome. Consequently, we analyzed HeLa cell lysate using mass spectrometry. The results revealed a notable presence of alpha-smooth muscle actin (α-SMA), which belongs to class 2 actins, under hypoxic conditions (Fig. S9). This protein is one of the key representatives of the Arg/*N*-degron pathway described earlier [30]. Thus, α-SMA could be a strong candidate among proteins that reacts by DNFC. The successful completion of this mass spectrometry analysis indicates that we are getting closer to the identification of *N*-degron biomarkers through DNFC.

2.5. DNFC enhancement in various cell types under hypoxic conditions

We further compared the DNFC fluorescence intensities of various cell types in normoxia and in hypoxia. All the tested cell types, *NIH-3T3* (mouse fibroblast cells), *CPAE* (calf artery endothelial cells), phorbol myristate acetate (PMA)-activated *THP-1* (human-derived macrophage cells) and *hMSC* (human mesenchymal stem cells), showed significant increase of the DNFC fluorescence in hypoxia compared to those in normoxia (Fig. 3i). Among the tested cells, the activated *THP-1* cells showed the largest increase of the fluorescence intensity by the hypoxia induction (Fig. 3i). Among these cell types, activated *THP-1* cells in hypoxia was dramatically decreased by the treatment of maleimide (MaI), a thiol blocking reagent (Fig. 3j), which strongly supported that the remarkable increase of the DNFC fluorescence in hypoxia was attributed to the increase of *N*-Cys in the cellular proteome.

The intracellular distribution of the DNFC fluorescence varied according to the cell types. Remarkably, cytosolic droplets were heavily stained in the activated *THP-1* cells (Fig. S10a) unlike *HeLa* cells showing stronger fluorescence in the nuclei by the DNFC process (Fig. 3a). Since the hypoxia exposure can promote the macrophage polarization to M2 phenotypes [31], we compared the DNFC fluorescence intensities of M1-and M2-polarized *THP-1* cells under hypoxic conditions (Figs. S10b–d). The findings suggest that activated *THP-1* cells, which show dramatic increases in DNFC fluorescence, exhibit characteristics similar to M2-polarized macrophages. Among potential *N*-Cys proteins generated by the Arg/*N*-degron pathway (Fig S 8), we propose that the regulator of G protein signaling 16 (RGS16) plays a critical role in the elevated DNFC fluorescence observed in hypoxic *THP-1* cells. Previous studies indicate that M2-inducing stimuli lead to a significant increase in RGS16 expression, modulating inflammatory responses [31–33]. Our experiments corroborate this, revealing approximately a 2-fold increase in RGS16 expression in *THP-1* cells under both hypoxic and M2-polarized states (Fig. S10). This elevation in RGS16 levels may stem from reduced degradation due to impaired oxidation of *N*-Cys under hypoxia. Additionally, other RGS proteins, such as RGS4 and RGS5, can produce *N*-Cys following methionine cleavage (Fig. S8 and Table S2). Therefore, we anticipate that the levels of these proteins may also increase, contributing to enhanced DNFC fluorescence in hypoxic conditions. Notably, RGS4, known for its high expression in the brain, showed enhanced DNFC fluorescence and co-localization with anti-RGS4 antibody staining in *SK-N-SH* (human neuroblastoma) cells under hypoxic conditions (Fig. 3k).

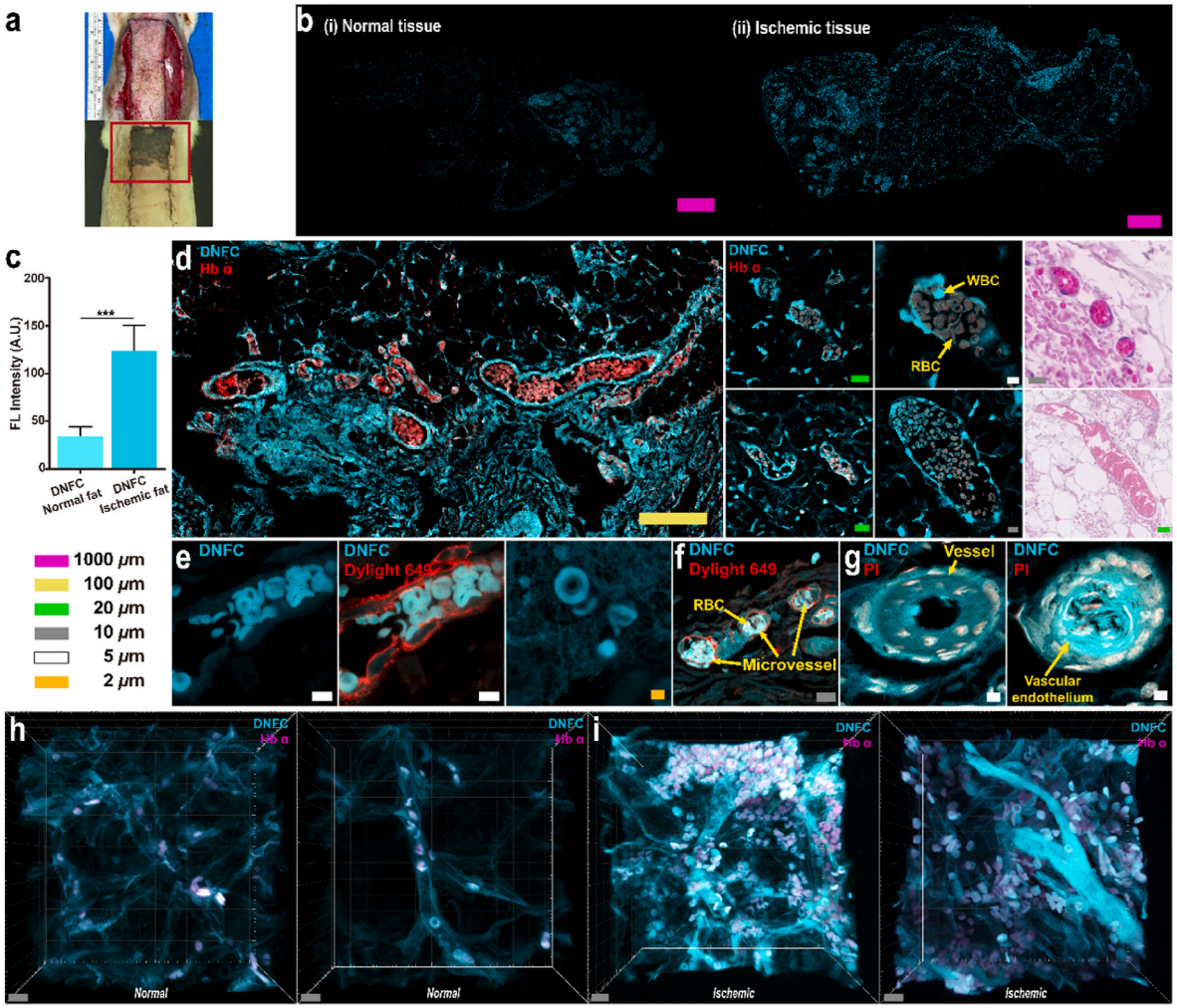

Fig. 4. Observation of DNFC-stained normal and ischemic rat subcutaneou**s tissues.** (a) The rat flap model post-induction (top) and before the tissue harvest (bottom). (b) Representative DNFC-stained rat subcutaneous tissue sections. (c) Comparison of DNFC fluorescence intensity of the normal and ischemic subcutaneous tissue sections. The fluorescence of three images were measured and averaged ($n = 3$). Each error bar represents S.D. *** indicates $0.0001 \leq p < 0.001$. (d) Representative magnified images of strongly DFNC-stained regions in the tissue sections. H&E-stained neighboring tissue sections are also shown for comparison. (e) Magnified images of RBCs in the vessels in the DNFC-stained tissue section. (f–g) Cross-sectional images of vessels in the DNFC-stained tissue section. Reconstructed 3D images of 100-μm-thick DNFC-stained (h) normal and (i) ischemic subcutaneous tissues. Pink, yellow, green, gray, white and orange scale bar represent 1000 μm, 100 μm, 20 μm, 10 μm, 5 μm and 20 μm, respectively.

As shown in various cell lines tested above, there is a clear enhancement of the DNFC fluorescence in hypoxia. Also, we observed a positive relationship between the DNFC fluorescence with the expression of two candidate *N*-Cys proteins, possibly up-regulated in hypoxia conditions. We would assess the relationship in more complexed levels, in rat, mouse or human tissues.

2.6. *Investigation of the increased DNFC fluorescence observed in specific structures of rat subcutaneous tissues under hypoxic conditions*

In previous studies, we observed that strong cyan fluorescence developed in DNFC-stained tissues, likely due to the expression of endogenous *N*-Cys proteins [20]. To compare fluorescence intensities between normal and ischemic tissues, we harvested subcutaneous tissues from a rat skin flap model (Fig. 4a) and stained both normal and ischemic subcutaneous tissues by the DNFC process (Fig. 4b). Remarkably, the ischemic tissue exhibited approximately three times stronger fluorescence intensity compared to the normal one (Fig. 4c and Fig. S11). Notably, lipid droplets in adipocytes were not stained, while protein-rich regions displayed strong staining (Fig. 4d, based on 2D imaging). Additionally, vascular structures were stained more intensely than surrounding areas, with both red blood cells (RBCs) and vascular walls showing pronounced staining within the vessels (Fig. 4e–g).

The remarkable increase of the DNFC fluorescence in RBCs and vascular walls was also clearly observed in 3D-reconstructed images of 100-μm-thick ischemic subcutaneous tissues (Fig. 4h and i, Fig S11, and Supporting Movie.1-4). Interestingly, while only limited RBC infiltration was observed in the normal adipose tissue, large numbers of RBCs were observed around the adipocytes in the ischemic tissue.

The stronger DNFC fluorescence in RBCs and vascular walls might be related to the vulnerability of endothelial cells and RBCs to hypoxia due to the redox signaling and ROS [34]. We could suggest possible candidate *N*-Cys proteins in the RBCs and the vascular walls for the increase of the DNFC fluorescence in hypoxia as RGS5 and a α-SMA. Both proteins possess *N*-Met-Cys sequences (Table S2), which could produce *N*-Cys by the Arg/*N*-degron pathway.

RGS5 has been reported to be prominently expressed in blood vessels during angiogenesis and in vascular endothelial cells under hypoxic

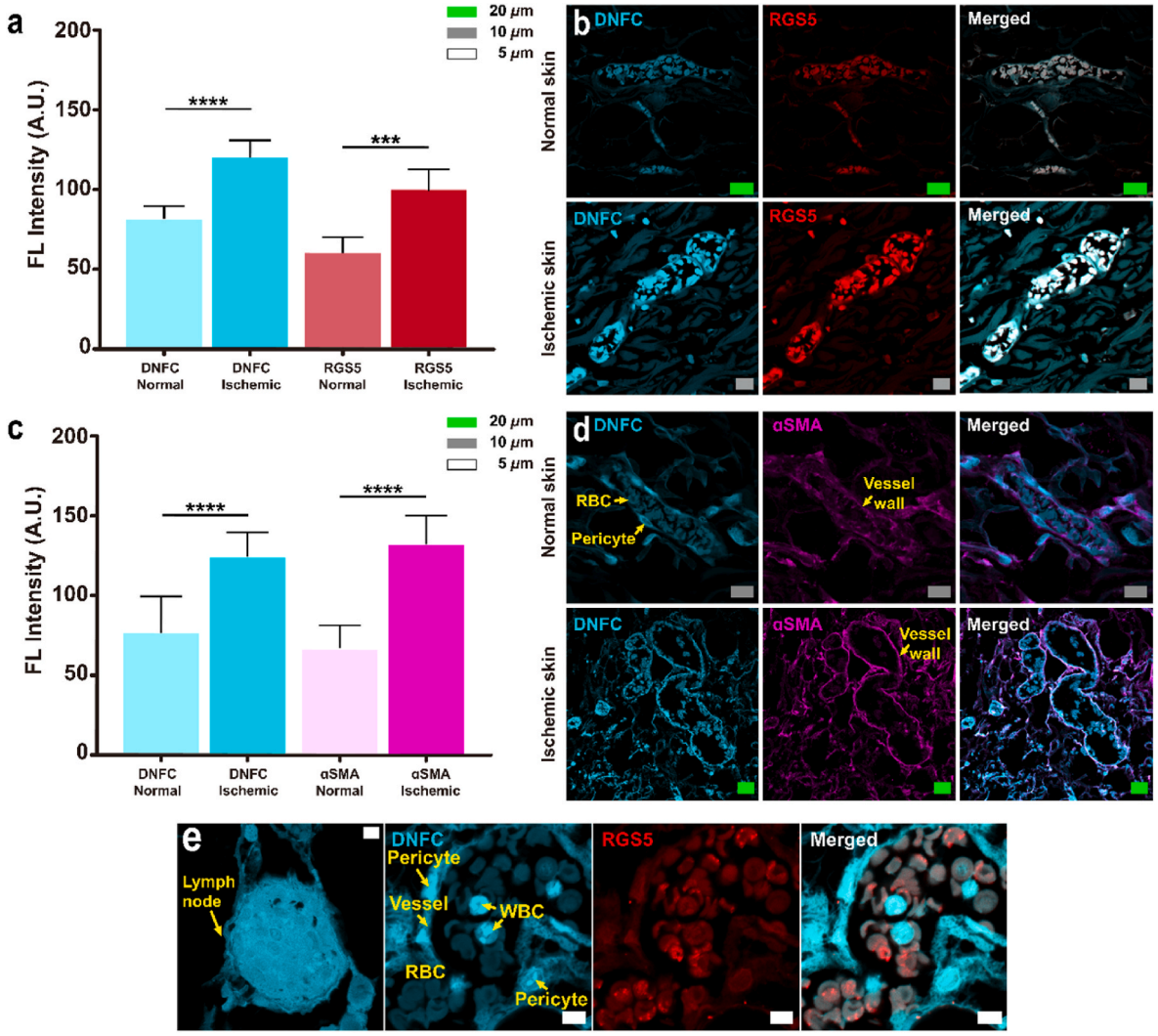

Fig. 5. Expression of RGS5 and αSMA in normal and ischemic rat subcutaneous tissues. (a) Comparison of DNFC fluorescence intensity and RGS5 expression in normal and ischemic subcutaneous tissue sections. The fluorescence of three images were measured and averaged ($n = 3$). (b) Co-localization of the DNFC fluorescence and RGS5 expression in normal and ischemic subcutaneous tissue sections. (c) Comparison of DNFC fluorescence intensity and α-SMA expression in normal and ischemic subcutaneous tissue sections. The fluorescence of three images were measured and averaged ($n = 3$). (d) Co-localization of the DNFC fluorescence and α-SMA expression in normal and ischemic subcutaneous tissue sections. (e) Magnified images of a lymph node, pericytes and blood cells in the ischemic subcutaneous tissue sections. DNFC fluorescence was obtained in the range of 410–550 nm ($\lambda_{ex} = 405$ nm). Each error bar represents S.D. *** and **** indicate $0.0001 \leq p < 0.001$ and $p < 0.0001$, respectively. Green, gray and white scale bars represent 20 μm and 10 μm and 5 μm, respectively.

conditions [35,36]. In our experiments, ischemic tissues exhibited approximately 2-fold stronger RGS5 signals than normal tissues (Fig. 5a). When we co-stained the tissue by immunostaining with anti-RGS5 antibodies and by the DNFC process, the RGS5 signal (red) also showed strong co-localization with the DNFC signal (cyan) (Fig. 5b). Interestingly, the RGS5 signal was observed more strongly in RBCs rather than in the vascular wall. The higher RGS5 expression in hypoxic RBCs has not been reported yet, but we envision that the phenomenon is related to the *N*-Cys of RGS5.

We also examined the co-localization of DNFC fluorescence with α-SMA expression in subcutaneous tissue. Ischemic tissue showed approximately 2-fold stronger α-SMA expression compared to normal tissue (Fig. 5c). Predominant α-SMA expression and its co-localization with DNFC signals were notably observed in the vascular walls, in contrast to the distribution of RGS5 (Fig. 5d). α-SMA, a class 2 actin highly expressed in smooth muscle tissues, is closely associated with vascular remodeling under hypoxic conditions. Furthermore, the *N*-terminal processing of α-SMA is known to involve methionine aminopeptidase, which can expose the *N*-Cys [30,37,38].

In lymph nodes and vessels within subcutaneous tissues, white blood cells and pericytes were also heavily stained by the DNFC process (Fig. 5e). Based on co-localization results, this strong staining appeared to have minimal association with RGS5 or α-SMA expression.

CLSM observations of rat subcutaneous tissues revealed a significant increase in DNFC fluorescence in ischemic conditions, alongside a pronounced co-localization of DNFC signals with Cys-containing proteins

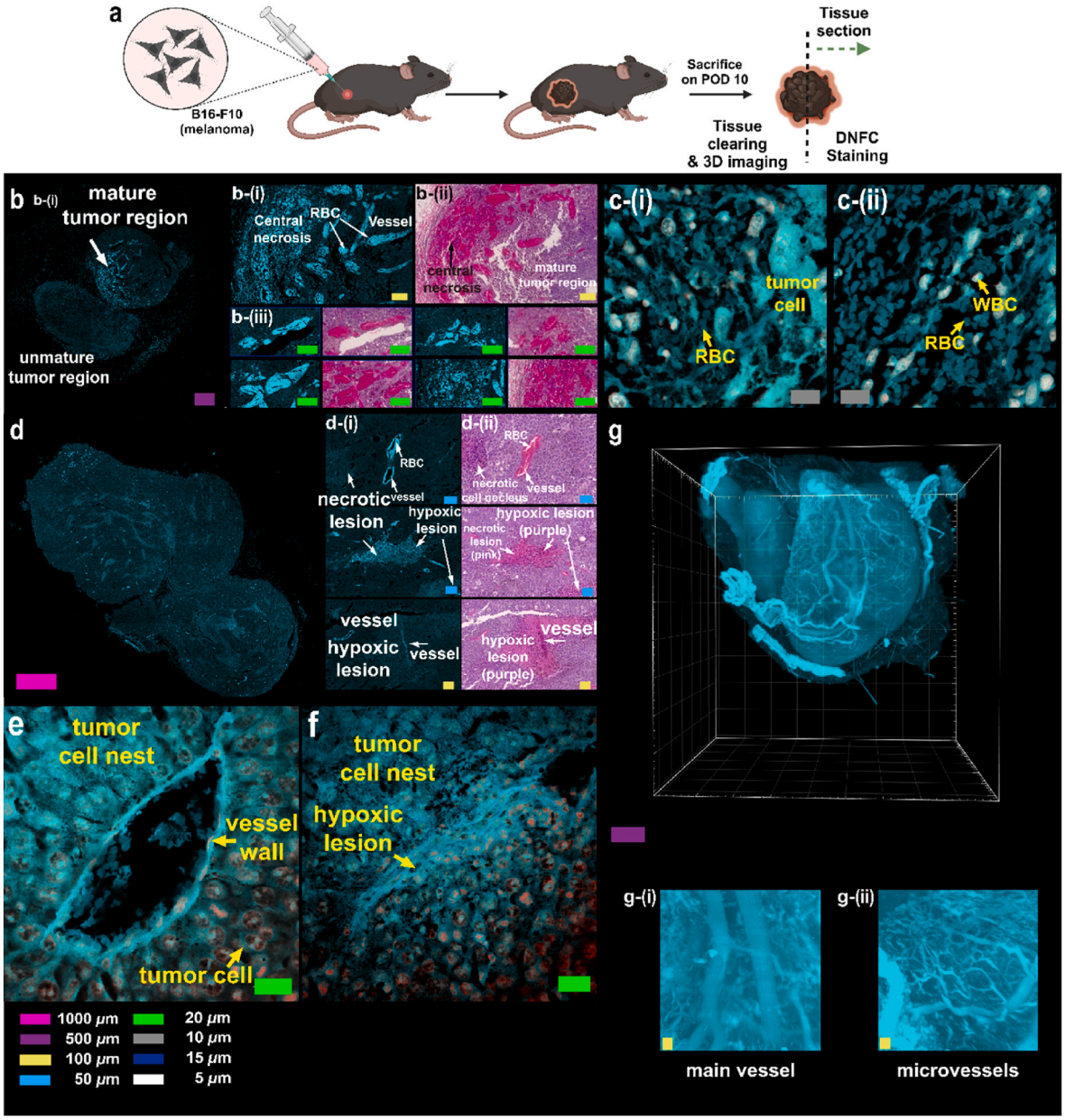

Fig. 6. Observation of DNFC-stained mouse xenograft melanoma. (a) The simplified scheme for the melanoma xenograft model and harvest. (b) A representative DNFC-stained mouse xenograft melanoma tissue section. Strongly stained regions are shown as magnified images. H&E-stained neighboring tissue sections are also shown for comparison. (c) Magnified Aryscan images of central necrosis regions in the melanoma tissue section. (d) Another representative DNFC-stained mouse xenograft melanoma tissue section. Strongly stained regions are shown as magnified images. H&E-stained neighboring tissue sections are also shown for comparison. Magnified Aryscan images of (e) the tumor cell nest around the vessel wall and (f) the hypoxic lesion in the melanoma tissue section. (g) A reconstructed 3D image of the DNFC-stained melanoma tissue with a size of 600 μm × 700 μm × 800 μm examined by the LSFM. Magnified images of the main vessels and microvessels in the tumor are also shown.

RGS5 and α-SMA, particularly in RBCs and vascular walls. Although the detailed mechanism has not been known yet, the stabilization of exposed *N*-Cys proteins may play critical roles in ischemic tissues.

2.7. Image analysis of DNFC-stained xenograft melanoma in mice

Given the close relationship between the microenvironment of rapidly growing tumors and hypoxia [39], we examined the intratumoral structures of melanoma generated by xenografting *B16–F10* cells onto the dorsal skin of mice (Fig. 6a). The fluorescence intensity was generally increased after the DNFC staining (Fig. S12) and certain regions were stained more strongly than other regions in the tumor (Fig. 6b–f). Strongly stained regions were identified by comparing them to adjacent slide sections stained with hematoxylin and eosin (H&E). Notably, vascular walls, along with red and white blood cells, demonstrated robust staining within the tumor tissue, resembling patterns observed in rat subcutaneous tissues (Fig. 4). Notably, the necrotic lesions, which are shown as pink in the H&E-stained images, also emitted stronger cyan fluorescence than other parts in the DNFC stained images (Fig. 6b and e). Among the tumor cells, which were stained as violet in the H&E-stained images, those in the tumor cell nest with high cell density showed stronger cyan fluorescence intensity than other tumor cells (Fig. 6e and f). The fluorescence intensity of the stasis zone between necrotic lesions and tumor cells was in the range between those of necrotic lesions and tumor cells (Fig. 6d). Rapid growth and hypoxic stress in the tumor microenvironments often induce central necrosis in the tumor [40,41]. These findings suggest that hypoxic necrotic lesions and dense tumor cell nests are more strongly stained by DNFC, reflecting the dynamic interplay of hypoxia and tumor growth.

The fluorescence-based staining can be readily combined with tissue-clearing techniques for 3D imaging of thick tissue samples, unlike absorbance-based H&E staining which can be generally used for 2D imaging of thin slides [42,43]. In our previous study, the DNFC staining could be combined with an organic solvent-based tissue-clearing method, 3D imaging of solvent-cleared organs (3DISCO) with CLSM [21]. However, for rapid 3D imaging with light sheet fluorescence microscopy (LSFM), we rather integrated the DNFC staining with an aqueous-based fast tissue-clearing method, optimized single-step optical clearing method (OptiMus) [44]. The DNFC-stained melanoma tissue can be cleared with the OptiMUS solution containing Iohexol, D-sorbitol

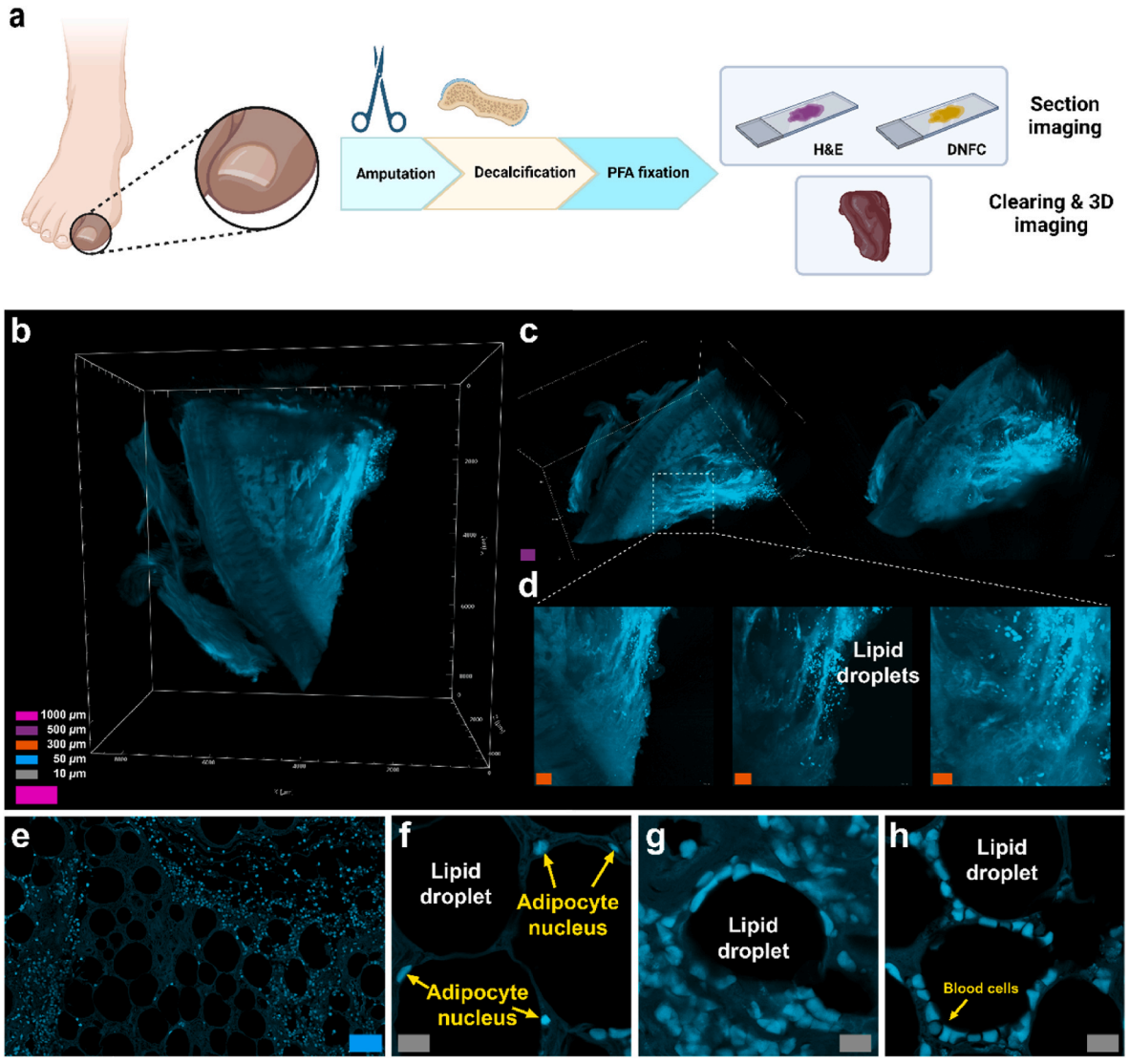

Fig. 7. Observation of DNFC-stained human diabetic foot ulcer (DFU) tissue. (a) The simplified scheme for the harvest, staining and observation of human DFU tissue. (b) A reconstructed 3D image of the DNFC-stained DFU tissue with a size of 4 mm × 5 mm × 8 mm examined by the LSFM. (c) A side view of the DNFC-stained DFU tissue. (d) Magnified images of strongly stained regions in the reconstructed 3D image. (e) A representative DNFC-stained DFU tissue section examined by the CLSM. (f–h) Magnified Aryscan images of the DFU tissue section. DNFC fluorescence was obtained in the range of 410–550 nm (λ_{ex} = 405 nm).

and urea for rapid 3D scanning with LSFM.

The 3D image of the DNFC-stained melanoma tissue with a size of 600 μm × 700 μm × 800 μm is shown in Fig. 6g, Fig. S12 and Supporting Movie. 5. The vessels are strongly stained in the tumor tissue, probably due to RBCs and vascular walls. The main vessels int the tumor inside and the chaotic network of the microvessels could be clearly observed in the 3D-scanned image. We expect that the 3D-imaging-based histopathology may provide many critical volumetric information by integrating the DNFC staining and the tissue clearing techniques in the future.

2.8. Image analysis of DNFC-stained human diabetic foot ulcer

We applied the DNFC staining strategy to the imaging analysis of a human diabetic foot ulcer (DFU) sample, given the established link between ischemia, hypoxia, and delayed wound healing in DFU [45,46]. The DFU tissue could be visualized in a 3D-manner by combination of the DNFC staining and the OptiMus tissue clearing (Fig. 7a). A 3D image of the DFU tissue, measuring 4 mm × 5 mm × 8 mm, was rapidly obtained using light-sheet fluorescence microscopy (LSFM) (Fig. 6b–d and Supporting Movie 6). The DNFC staining effectively revealed the general 3D morphology of the DFU tissue, with stronger staining observed in the epidermis compared to the dermis. This resulted in a distinct wave-like pattern at the dermal-epidermal junction. Notably, particle-like structures were prominently stained within the subcutaneous tissue, identified as infiltrated RBCs by comparing 2D-sectioned slides (Fig. 7e–h and Fig. S13).

The hypoxic condition of the DFU tissue seems to be connected to the distinct RBC infiltration. While hypoxia normally stimulates angiogenesis to recruit extra RBCs for oxygen delivery, hyperglycemia might damage microvascular function, aggravating immune cell infiltration. Furthermore, erythrocyte extravasation and capillary leakage might result from damage to vertical arterioles and capillaries caused by hypoxia-related microangiopathy [47]. The accumulation of strongly stained RBCs may reflect impaired vascular structures and congestion of dysfunctional RBCs in hypoxic DFU tissue. This is corroborated by observations of petechiae and skin dyschromia in many DFU patients, indicative of injuries to terminal microvascular structures (Fig. S13). The characteristic accumulation of RBCs in hypoxic conditions was also evident in 3D imaging of subcutaneous tissue from a rat flap model (Fig. 4, Fig. S11, and Supporting Movie 1-4), suggesting that bright staining of infiltrated RBCs could serve as a useful indicator for 3D histopathology of ischemic adipose tissues.

3. Conclusion

In this study, we confirmed that the fluorescent thiazolopyridine (TPA) structure can be selectively generated on cysteine (Cys)-containing molecules in biological samples through condensation reactions with citrate (Fig. 1). At the amino acid, peptide, and protein levels, fluorescence intensity increased with *N*-Cys content, essential for thiazolopyridine ring formation in TPA structures. DNFC treatment induced cyan fluorescence in *N*-Cys proteins, further enhanced by exogenous *N*-Cys and hypoxia, offering a strategy for targeted visualization and analysis of *N*-Cys protein expression. The Arg/*N*-degron pathway may play a crucial role in the elevation of *N*-Cys levels under these conditions (Fig. S8). This process begins with the cleavage of the *N*-Met by methionine aminopeptidase. A protein with Cys at the P2 position can expose *N*-Cys upon cleavage of the methionine. The exposed Cys undergoes oxidation in the presence of oxygen, and the oxidized Cys is recognized and subsequently arginylated by arginyltransferase. Arginylated proteins are then degraded by the ubiquitin-proteasome system (UPS). However, under hypoxic conditions, Cys oxidation and UPS-dependent degradation are impaired, allowing proteins with *N*-Cys to accumulate. We propose a list of proteins expected to expose *N*-Cys through the Arg/*N*-degron pathway (Table S2). Among these potential candidate proteins, RGS16, RGS4, RGS5, and α-SMA exhibited significantly stronger expression in *THP-1* cells, RBCs, and vascular walls under hypoxia, respectively (Figs. 3–7). Notably, the high expression of RGS5 in hypoxic RBCs represents a novel finding, as this protein is predominantly found in vascular tissues. Moreover, the identification of α-SMA through mass spectrometry highlights it as a promising candidate protein, suggesting its application in the observation of various related diseases.

Additionally, the general facilitation of protein degradation may expose the amino group of Cys within the protein structure, statistically increasing the level of *N*-Cys in the resulting fragments. Given that various endopeptidases could be activated under stress conditions such as hypoxia or inflammation, this could be one reason for the increased DNFC signals observed in hypoxic environments. The substantial increase in DNFC fluorescence observed in hypoxic tissues points to a possible diagnostic approach for disorders associated with hypoxia, such as strokes, malignancies, and diabetic foot ulcers (DFU). Furthermore, DNFC staining is compatible with tissue clearing techniques, such as 3DISCO and OptiMus, enabling rapid 3D imaging of thick tissues. We demonstrated its applicability in 3D imaging of mouse xenograft melanoma and human clinical DFU tissues with dimensions in the millimeter range (Figs. 6–7 and Supporting Movies 5-6). The 3D LFSM imaging of cleared tissues allowed for swift examination of hypoxic tumor cell nests and the complex vascular networks within tumor tissues, as well as strong infiltration of blood cells into the subcutaneous adipose tissue in DFU samples. The DNFC method allows for rapid and cost-effective staining of thick tissues while providing quantitative information on *N*-Cys levels, alongside analysis of the overall tissue structure. This study has linked DNFC staining, dependent on the distribution of *N*-Cys, to hypoxic levels. While the biological role of *N*-Cys has been primarily associated with the regulation of protein degradation in the Arg/*N*-degron pathway, the detailed spatial information obtained through DNFC staining-based imaging could aid in investigating the unknown roles of *N*-Cys proteins and discovering novel biomarkers related to biological redox potentials. Furthermore, through future collaborations with histologists, DNFC staining-based volumetric imaging could be developed as a novel method for 3D histopathology, particularly in the prognosis and diagnosis of hypoxia-related diseases.

4. Materials and methods

4.1. General procedure for the TPA formation by the DNFC method

For the TPA formation in the amino acid mixture, citric acid monohydrate (0.200 g, 0.952 mmol, 1.00 eq.) was dissolved in dimethylsulfoxide (DMSO) (1.0 mL) and *N,N*-diisopropylethylamine (DIPEA) (162 μL, 0.952 mmol, 1.00 eq.) was added to the solution. Benzotriazole-1-yl-oxy-tris-pyrrolidino-phosphonium hexafluorophosphate (PyBOP) (0.496 g, 0.952 mmol, 1.00 eq.) in DMSO (2.0 mL) was added to the citric acid solution. An amino acid (0.952 mmol, 1.00 eq.) in DMSO (1.0 mL) was added to the yellowish solution. The mixture was incubated while stirring at an ambient temperature. After incubation for some time, the mixture was analyzed with a spectrophotometer and a spectrofluorometer or purified by high-performance liquid chromatography (HPLC).

For the TPA formation in the tripeptide mixture, citric acid monohydrate (4.2 mg, 20 μmol, 20.0 eq.) was dissolved in deionized water (120 μL), and DIPEA (162 μL, 20 μmol, 20.0 eq.) was subsequently added to the solution. PyBOP (0.496 g, 20 μmol, 20.0 eq.) in DMSO (280 μL) was introduced to the citric acid solution. The mixture was added with a tripeptide (2–8 μmol) in a PBS buffer, incubated at ambient temperature. The crude mixture was analyzed directly for the fluorescence measurement.

For the TPA formation in the eGFP mixture, a citrate solution containing citric acid monohydrate (70 mg, 0.32 mmol), DIPEA (60 μL, 0.32 mmol) and PyBOP (175 mg, 0.32 mmol) in 1 mL of DMSO was

prepared. eGFPs with different *N*-termini were separately dissolved in DPBS. The protein solution was mixed with the citrate solution and diluted with 75% DMSO/water. The final concentrations of the proteins were varied in the range of 1.1–3.3 μM, whereas the final concentrations of citrate, DIPEA and PyBOP were maintained as 3.2 mM. The crude mixture was incubated for some time at ambient temperature and measured directly for the fluorescence measurement.

4.2. Fixation and staining of various cells

Cells in a slide chamber were fixed with 4% paraformaldehyde (PFA) for 10 min. After reduction with 0.1% sodium borohydride in DPBS for 7 min, the cells were treated with 100 mM glycine in DPBS for 10 min for quenching. The cells were washed with PBS three times for 5 min each. All the fixation process was performed at ambient temperature.

The fixed cells were stained by the DNFC process. Citric acid monohydrate (0.10 g, 0.48 mmol) was dissolved in 60% DMSO/water (1.0 mL) and DIPEA (81 μL, 0.48 mmol) was added to the solution. PyBOP (0.25 g, 0.48 mmol) in DMSO (1.0 mL) was added to the citric acid solution. The mixture was added to the fixed cells. After incubation for 1 h at ambient temperature, the cells were successively washed with 70% DMSO ($\times$ 3), 50% DMSO ($\times$ 3) and PBS ($\times$ 3).

The DNFC-stained cells could be additionally stained with antibodies. The cells were permeabilized with PBS containing 0.1% Triton X-100 (PBST) for 30 min at ambient temperature. After washing with PBST three times for 5 min each, the cells were treated with a blocking buffer (1% BSA dissolved in PBST) for 30 min at ambient temperature. Then, a primary antibody was treated to the permeabilized cells. After incubation for overnight at 4°C, the cells were washed with the blocking buffer for 5 min ($\times$ 3). A fluorophore-labeled secondary antibody was treated to the cells and incubated in the dark for 2 h at ambient temperature. The cells were washed with the blocking buffer for 5 min ($\times$ 3).

For propidium iodide (PI) staining, a PI solution diluted with PBST was added to the DNFC-stained cells and incubated for 10 min. After washing with the blocking solution for 5 min ($\times$ 3), the sample was further washed with PBS until the surfactant is completely removed.

4.3. Hypoxia induction

Hypoxia was induced by the treatment of cells with cobalt chloride ($CoCl_2$) at the final concentration of 200 μM. The cells were incubated at 37°C in a 5% CO_2 incubator before the DNFC staining. In an experiment, *N*-acetyl cysteine (NAC), a hypoxia inhibitor, was additionally treated to the cells at a concentration of 2 mM for 24 h simultaneously with $CoCl_2$ treatment. After the hypoxia induction, the cells were washed thoroughly and stained by the DNFC process as described above. For the thiol blocking experiments, a maleimide solution in DMSO was pretreated to the fixed cells at the concentration of 1 mM for 4 h at 37°C before the DNFC staining.

4.4. CLSM observation

The CLSM images were obtained by the LSM710 system (Carl Zeiss, Germany) installed at the National Center for Inter-university Research Facilities (NCIRF) at Seoul National University. Blue channel images (410–500 nm) and green channel images (500–550 nm) were acquired with excitation at 405 nm to capture the DNFC-based fluorescence signals. On the other hand, images in the 650–700 nm channel, achieved by excitation at 639 nm, were obtained to capture the Alexa fluor® 647 signals. Images in the 600–620 nm channel were acquired with excitation at 561 nm to capture the PI signals. Additionally, images in the 660–700 nm channel were acquired with excitation at 639 nm to capture the Dylight 649 signals.

4.5. Animal models and human samples

Detailed procedures for the animal experiments are described in Supporting Information. The animal experiments using the rat skin flap model and the mouse melanoma xenograft model were approved by the Institutional Animal Care and Use Committee (IACUC) of the Seoul National University Boramae Hospital (approval No. 2023-0053 and 2023-0018, respectively). Human diabetic foot tissues were collected at the Department of Plastic and Reconstructive Surgery, Seoul National University Boramae Hospital (IRB No. 26-2016-180).

4.6. DNFC staining of tissue samples

For the DNFC staining, citric acid monohydrate (0.10 g, 0.48 mmol) was dissolved in 50% *N*,*N*-dimethylformamide (DMF)/water (1.0 mL) and DIPEA (81 μL, 0.48 mmol) was added to the solution. PyBOP (0.25 g, 0.48 mmol) in DMF (1.0 mL) was added to the citric acid solution. Tissue sections were placed in the solution and incubated for 2 h at ambient temperature in the dark without agitation. The DNFC-stained tissue samples could be stained with antibodies or PI through similar processes described above.

4.7. 3D observation of tissues

Microsectioned tissue samples with a thickness of 100 μm were observed by the CLSM. For the observation of thick tissue samples, the harvested tissues were subjected to a PFA fixation for 24 h [48]. The samples were dehydrated using DMF/water with ascending concentrations of DMF (25%, 50%, and 75%). The samples were stained with the DNFC staining solution at 37°C for 1 day. After thoroughly replacing the staining solution with water, the DNFC-stained tissues were immersed in the OptiMus clearing solution for two days. For the preparation of the clearing solution, the Histodenz solution was initially prepared by dissolving iohexol at a concentration of 75% (w/v) in a Tris-EDTA buffer (100 mM Tris, 0.5 mM EDTA, pH 7.5) at 60°C. After obtaining the transparent Histodenz solution, D-sorbitol and urea were added to the solution at 60°C to adjust the final concentrations of 10% (w/v) and 4 M, respectively. The OptiMus clearing solution was cooled to ambient temperature for the clearing of the tissue sample [44]. For clearing of the melanoma tissue sample, a bleaching step for the removal of melanin pigments with 7.5% hydrogen peroxide was required. The bleaching process was described in detail in the Supporting Information.

The LSFM images of the cleared tissue samples were acquired using the Lightsheet 7 (Carl Zeiss, Germany) with an EC Plan-Neofluar 5 $\times$ /0.16 objective and a 5 $\times$ clarity chamber at 405 nm laser. Whole DNFC-stained tissue images were merged with a 10% overlap of tiles using the Arivis software (Munich, Germany).

CRediT authorship contribution statement

Yunjung Choi: Writing – original draft, Visualization, Validation, Methodology, Investigation, Formal analysis. **Joo-Yeong Jeon:** Writing – original draft, Visualization, Software, Investigation. **Jeongin Hwang:** Writing – original draft, Resources. **Sejong Choi:** Resources. **Ki-Myo Kim:** Writing – original draft, Resources, Formal analysis. **Ji-Ung Park:** Writing – review & editing, Resources, Investigation. **Yan Lee:** Writing – review & editing, Supervision, Conceptualization.

Declaration of competing interest

The authors declare that they have no known competing financial interests or personal relationships that could have appeared to influence the work reported in this paper.

Acknowledgment

The authors would like to express our appreciation to Ph.D. candidate researcher Kitae Kim at Seoul National University College of Medicine advising on OptiMUS solution and facilitating access to the Zeiss Lightsheet7 demonstration equipment. Additionally, we are grateful to the Korea Basic Science Institute (KBSI) and Bruker for their support with protein mass analysis. This work was supported by NRF-2022M3H9A2083956, NRF-2022M3A9F3017371 and RS-2023-00217942 from the National Research Foundation of Korea.

Appendix A. Supplementary data

Supplementary data to this article can be found online at https://doi.org/10.1016/j.redox.2025.103577.

Data availability

Data will be made available on request.

References

[1] Y.L. Pak, K.M. Swamy, J. Yoon, Recent progress in fluorescent imaging probes, Sensors 15 (9) (2015) 24374–24396.
[2] C. Li, A.G. Tebo, A. Gautier, Fluorogenic labeling strategies for biological imaging, Int. J. Mol. Sci. 18 (7) (2017).
[3] Y. Yang, F. Gao, Y. Wang, H. Li, J. Zhang, Z. Sun, Y. Jiang, Fluorescent organic small molecule probes for bioimaging and detection applications, Molecules 27 (23) (2022).
[4] S.Y. Mao, J.M. Mullins, Conjugation of fluorochromes to antibodies, Methods Mol. Biol. 588 (2010) 43–48.
[5] E.V. Dolgosheina, S.C. Jeng, S.S. Panchapakesan, R. Cojocaru, P.S. Chen, P. D. Wilson, N. Hawkins, P.A. Wiggins, P.J. Unrau, RNA mango aptamer-fluorophore: a bright, high-affinity complex for RNA labeling and tracking, ACS Chem. Biol. 9 (10) (2014) 2412–2420.
[6] A. Autour, C.Y.J. S, D.C. A, A. Abdolahzadeh, A. Galli, S.S.S. Panchapakesan, D. Rueda, M. Ryckelynck, P.J. Unrau, Fluorogenic RNA Mango aptamers for imaging small non-coding RNAs in mammalian cells, Nat. Commun. 9 (1) (2018) 656.
[7] L. Mendive-Tapia, J.L. Wang, M. Vendrell, Fluorescent cyclic peptides for cell imaging, Peptide Sci. 113 (1) (2021).
[8] B. Jandl, S. Sedghiniya, A. Carstens, K. Astakhova, Peptide-fluorophore hydrogel as a signal boosting approach in rapid detection of cancer DNA, ACS Omega 4 (9) (2019) 13889–13895.
[9] B. Huang, W. Wang, M. Bates, X. Zhuang, Three-dimensional super-resolution imaging by stochastic optical reconstruction microscopy, Science 319 (5864) (2008) 810–813.
[10] A.K. Gustavsson, P.N. Petrov, M.Y. Lee, Y. Shechtman, W.E. Moerner, 3D single-molecule super-resolution microscopy with a tilted light sheet, Nat. Commun. 9 (1) (2018) 123.
[11] M. Belle, D. Godefroy, G. Couly, S.A. Malone, F. Collier, P. Giacobini, A. Chedotal, Tridimensional visualization and analysis of early human development, Cell 169 (1) (2017) 161–173e12.
[12] E.C. Costa, D.N. Silva, A.F. Moreira, I.J. Correia, Optical clearing methods: an overview of the techniques used for the imaging of 3D spheroids, Biotechnol. Bioeng. 116 (10) (2019) 2742–2763.
[13] J. Chan, S.C. Dodani, C.J. Chang, Reaction-based small-molecule fluorescent probes for chemoselective bioimaging, Nat. Chem. 4 (12) (2012) 973–984.
[14] R. Piña, A.I. Santos-Díaz, E. Orta-Salazar, A.R. Aguilar-Vazquez, C.A. Mantellero, I. Acosta-Galeana, A. Estrada-Mondragon, M. Prior-Gonzalez, J.I. Martinez-Cruz, A. Rosas-Arellano, Ten approaches that improve immunostaining: a review of the latest advances for the optimization of immunofluorescence, Int. J. Mol. Sci. 23 (3) (2022).
[15] R.J. Mailloux, R. Beriault, J. Lemire, R. Singh, D.R. Chenier, R.D. Hamel, V. D. Appanna, The tricarboxylic acid cycle, an ancient metabolic network with a novel twist, PLoS One 2 (8) (2007) e690.
[16] K. El-Dawy, A.S.A. El-Sayed, S.A. El-Hefnawy, N.M. El-Kahky, Biochemical and metabolic implications of tricarboxylic acids and their transporters, J. Pure Appl. Microbiol. 13 (2) (2019) 757–766.
[17] W. Kasprzyk, S. Bednarz, D. Bogdal, Luminescence phenomena of biodegradable photoluminescent poly(diol citrates), Chem. Commun. 49 (57) (2013) 6445–6447.
[18] Z. Xie, J.P. Kim, Q. Cai, Y. Zhang, J. Guo, R.S. Dhami, L. Li, B. Kong, Y. Su, K. A. Schug, J. Yang, Synthesis and characterization of citrate-based fluorescent small molecules and biodegradable polymers, Acta Biomater. 50 (2017) 361–369.
[19] J. Yang, Y. Zhang, S. Gautam, L. Liu, J. Dey, W. Chen, R.P. Mason, C.A. Serrano, K. A. Schug, L. Tang, Development of aliphatic biodegradable photoluminescent polymers, Proc. Natl. Acad. Sci. U. S. A. 106 (25) (2009) 10086–10091.
[20] D. Jung, D. Choi, C. Sim, Y. Kim, S. Kang, S.H. Nam, J. Jang, D. Kim, M.S. Chang, J. U. Park, Y. Lee, De novo formation of citrate-based fluorophores on N-termini of peptides and proteins in cells and tissues, Chem. Commun. 56 (1) (2020) 74–77.
[21] J. Pac, D.J. Koo, H. Cho, D. Jung, M.H. Choi, Y. Choi, B. Kim, J.U. Park, S.Y. Kim, Y. Lee, Three-dimensional imaging and analysis of pathological tissue samples with de novo generation of citrate-based fluorophores, Sci. Adv. 8 (46) (2022).
[22] J.M. Lee, H.M. Hammaren, M.M. Savitski, S.H. Baek, Control of protein stability by post-translational modifications, Nat. Commun. 14 (1) (2023) 201.
[23] L. Chen, A. Kashina, Post-translational modifications of the protein termini, Front. Cell Dev. Biol. 9 (2021) 719590.
[24] A.J. Heo, S.B. Kim, C.H. Ji, D. Han, S.J. Lee, S.H. Lee, M.J. Lee, J.S. Lee, A. Ciechanover, B.Y. Kim, Y.T. Kwon, The N-terminal cysteine is a dual sensor of oxygen and oxidative stress, Proc. Natl. Acad. Sci. U. S. A. 118 (50) (2021).
[25] A.J. Heo, C.H. Ji, Y.T. Kwon, The Cys/N-degron pathway in the ubiquitin-proteasome system and autophagy, Trends Cell Biol. 33 (3) (2023) 247–259.
[26] S. Choi, Y. Lee, J. Hwang, D. Chun, H. Koo, Y. Lee, Self-cleaving protein linkers with modulated pH-responsiveness: a new platform for selective control of protein drug function, Chem. Eng. J. 457 (2023).
[27] T. Tasaki, S.M. Sriram, K.S. Park, Y.T. Kwon, The N-end rule pathway, Annu. Rev. Biochem. 81 (2012) 261–289.
[28] S.P. Baba, A. Bhatnagar, Role of thiols in oxidative stress, Curr. Opin. Toxicol. 7 (2018) 133–139.
[29] J. Jiang, C. Auchinvole, K. Fisher, C.J. Campbell, Quantitative measurement of redox potential in hypoxic cells using SERS nanosensors, Nanoscale 6 (20) (2014) 12104–12110.
[30] S. Varland, J. Vandekerckhove, A. Drazic, Actin post-translational modifications: the cinderella of cytoskeletal control, Trends Biochem. Sci. 44 (6) (2019) 502–516.
[31] M. Jiang, G. He, J. Wang, X. Guo, Z. Zhao, J. Gao, Hypoxia induces inflammatory microenvironment by priming specific macrophage polarization and modifies LSC behaviour via VEGF-HIF1alpha signalling, Transl. Pediatr. 10 (7) (2021) 1792–1804.
[32] J. Suurvali, M. Pahtma, R. Saar, V. Paalme, A. Nutt, T. Tiivel, M. Saaremae, C. Fitting, J.M. Cavaillon, S. Ruutel Boudinot, RGS16 restricts the pro-inflammatory response of monocytes, Scand. J. Immunol. 81 (1) (2015) 23–30.
[33] M. Tian, Y. Ma, T. Li, N. Wu, J. Li, H. Jia, M. Yan, W. Wang, H. Bian, X. Tan, J. Qi, Functions of regulators of G protein signaling 16 in immunity, inflammation, and other diseases, Front. Mol. Biosci. 9 (2022) 962321.
[34] A. Mahdi, M.M. Cortese-Krott, M. Kelm, N. Li, J. Pernow, Novel perspectives on redox signaling in red blood cells and platelets in cardiovascular disease, Free Radic. Biol. Med. 168 (2021) 95–109.
[35] G.F. Lu, R. Du, Y.L. Liu, S.M. Zhang, J. Li, J.M. Pei, RGS5 as a biomarker of pericytes, involvement in vascular remodeling and pulmonary arterial hypertension, Vasc. Health Risk Manag. 19 (2023) 673–688.
[36] Y. Jin, X. An, Z. Ye, B. Cully, J. Wu, J. Li, RGS5, a hypoxia-inducible apoptotic stimulator in endothelial cells, J. Biol. Chem. 284 (35) (2009) 23436–23443.
[37] X.J. Huang, E.E. Akguen, K. Mehmood, H. Zhang, Z.X. Tang, Y. Li, Mechanism of hypoxia-mediated smooth muscle cell proliferation leading to vascular remodeling, BioMed Res. Int. 2022 (2022).
[38] J.H. Lee, H. Kang, Hypoxia promotes vascular smooth muscle cell proliferation through microRNA-mediated suppression of cyclin-dependent kinase inhibitors, Cells-Basel 8 (8) (2019).
[39] Y. Li, L. Zhao, X.F. Li, Hypoxia and the tumor microenvironment, Technol. Cancer Res. Treat. 20 (2021) 15330338211036304.
[40] Z. Chen, F. Han, Y. Du, H. Shi, W. Zhou, Hypoxic microenvironment in cancer: molecular mechanisms and therapeutic interventions, Signal Transduct. Targeted Ther. 8 (1) (2023) 70.
[41] T. Hompland, C.S. Fjeldbo, H. Lyng, Tumor hypoxia as a barrier in cancer therapy: why levels matter, Cancers 13 (3) (2021).
[42] A. Laurino, A. Franceschini, L. Pesce, L. Cinci, A. Montalbano, G. Mazzamuto, G. Sancataldo, G. Nesi, I. Costantini, L. Silvestri, F.S. Pavone, A guide to perform 3D histology of biological tissues with fluorescence microscopy, Int. J. Mol. Sci. 24 (7) (2023).
[43] I. Jansen, M. Lucas, C.D. Savci-Heijink, S.L. Meijer, H.A. Marquering, D.M. de Bruin, P.J. Zondervan, Histopathology: ditch the slides, because digital and 3D are on show, World J. Urol. 36 (4) (2018) 549–555.
[44] K. Kim, M. Na, K. Oh, E. Cho, S.S. Han, S. Chang, Optimized single-step optical clearing solution for 3D volume imaging of biological structures, Commun. Biol. 5 (1) (2022) 431.
[45] S.H. Wang, C.Y. Yin, X.G. Han, A.Y. Guo, X.D. Chen, S.J. Liu, Y.J. Liu, Improved healing of diabetic foot ulcer upon oxygenation therapeutics through oxygen-loading nanoperfluorocarbon triggered by radial extracorporeal shock wave, Oxid. Med. Cell. Longev. 2019 (2019).
[46] S.B. Catrina, X.W. Zheng, Disturbed hypoxic responses as a pathogenic mechanism of diabetic foot ulcers, Diabetes-Metab. Res. 32 (2016) 179–185.
[47] A. Caggiati, M. Franceschini, R. Heyn, C. Rosi, Skin erythrodiapedesis during chronic venous disorders, J. Vasc. Surg. 53 (6) (2011) 1649–1653.
[48] M.H. Choi, T.S. Jang, H. Kim, I. Ku, J. Lee, J.G. Jeong, S. Kim, J.U. Park, An agonistic monoclonal antibody targeting cMet attenuates inflammation and up-regulates collagen synthesis and angiogenesis in type 2 diabetic mice wounds, Plast. Reconstr. Surg. 150 (3) (2022) 572e–583e.